

A Micropower Electrocardiogram Amplifier

Leon Fay, Vinith Misra, and Rahul Sarpeshkar, *Senior Member, IEEE*

Abstract—We introduce an electrocardiogram (EKG) preamplifier with a power consumption of $2.8 \mu\text{W}$, $8.1 \mu\text{V}_{\text{rms}}$ input-referred noise, and a common-mode rejection ratio of 90 dB. Compared to previously reported work, this amplifier represents a significant reduction in power with little compromise in signal quality. The improvement in performance may be attributed to many optimizations throughout the design including the use of subthreshold transistor operation to improve noise efficiency, gain-setting capacitors versus resistors, half-rail operation wherever possible, optimal power allocations among amplifier blocks, and the sizing of devices to improve matching and reduce noise. We envision that the micropower amplifier can be used as part of a wireless EKG monitoring system powered by rectified radio-frequency energy or other forms of energy harvesting like body vibration and body heat.

Index Terms—Common-mode feedback (CMFB), electrocardiograph (ECG), electrocardiogram (EKG), low noise, low power.

I. INTRODUCTION

THE trend toward increasingly portable and even wearable medical devices demands smaller batteries. At the same time, frequent battery replacement is highly undesirable. Reduced power consumption can address both of these constraints. We seek such a reduction within the application area of electrocardiogram (EKG) monitoring.

An EKG measurement setup typically consists of the following:

- 1) electrodes at several points on the subject's body;
- 2) an analog front end (AFE) that amplifies the EKG signal gathered by the electrodes;
- 3) an analog-to-digital converter (ADC) that digitizes the amplified signal;
- 4) a display/processing unit that the user may interact with.

While EKG systems can be quite bulky, there has been recent interest in miniaturization and the introduction of wireless links between the ADC and the display/processing unit [1], [2]. Despite the reduced form factor of such a system, the user is required to carry and replace a battery.

However, if the AFE and ADC are sufficiently low power, it is conceivable for the battery to be partially or completely replaced by an radio-frequency identification (RFID) power

Manuscript received March 13, 2009; revised May 23, 2009. First published August 25, 2009; current version published September 25, 2009.

L. Fay is with SRI International, Menlo Park, CA 94025 USA (e-mail: leon.fay@gmail.com).

V. Misra is with the Department of Electrical Engineering, Stanford University, Stanford, CA 94305 USA (e-mail: vinith@stanford.edu).

R. Sarpeshkar is with the Department of Electrical Engineering and Computer Science, Analog VLSI and Biological Systems Group, Research Laboratory of Electronics, Massachusetts Institute of Technology (MIT), Cambridge, MA 02139 USA (e-mail: rahuls@mit.edu)

Color versions of one or more of the figures in this paper are available online at <http://ieeexplore.ieee.org>.

Digital Object Identifier 10.1109/TBCAS.2009.2026483

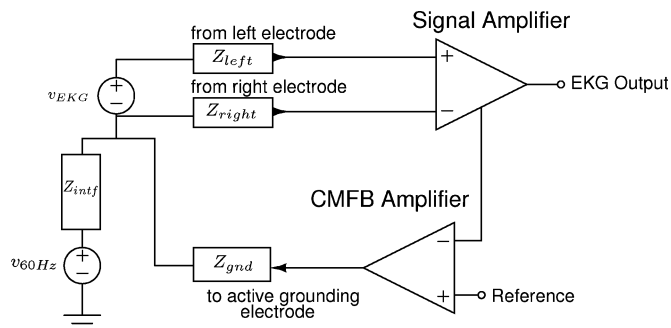


Fig. 1. Overall EKG amplifier topology.

extraction system or by other forms of energy harvesting, such as body vibration or body heat. It has been demonstrated that far-field RFID power can reliably create a battery with $6 \mu\text{W}$ of received RF power [3] and that analog-to-digital conversion for relatively slow biomedical signals may be performed for less than $1 \mu\text{W}$ [4], [5]. The bottleneck in power is the EKG amplifier or AFE. While several electroencephalogram (EEG) amplifiers and general-purpose biopotential amplifiers have been designed for low-power operation [6]–[10], these circuits do not possess active feedback grounding techniques that are important in practical EKG amplifiers for attenuating 60-Hz noise. These techniques also enable operation of differential EKG amplifiers with reduced requirements on common-mode rejection and common-mode operation, thus obviating the need for high-precision trimming and matching. We show that our implementation of active grounding enables $3\text{-}\mu\text{mW}$ operation while maintaining sufficient resolution of EKG waveform details necessary in a wireless monitoring application. For example, even P-wave information, which indicates atrial polarization and constitutes the smallest piece of an EKG waveform, is preserved. In some applications, where only heart-rate information is needed, power may be lowered even further if needed. Current EKG amplifier designs that incorporate active grounding consume $20 \mu\text{W}$ or more [11].

Fig. 1 depicts a block diagram of the EKG AFE. The differential EKG signal is collected by taking the amplified difference of electrode signals from two locations on the body. These locations may be the left arm and right arm, or in wireless monitoring applications may be two locations near the heart. Since the signal inputs occur at high impedance nodes, they often pick up a considerable amount of an interfering common-mode 60-Hz signal $V_{60 \text{ Hz}}$ that is nearly equal at all locations on the body. One solution to this problem is to connect the ground or a reference terminal in the amplifier to a third electrode on the body, which is often on the leg but more likely near the heart in a wireless monitoring application. While this passive grounding can be effective, it is limited by the fact that the grounding

electrode itself has significant impedance Z_{gnd} due to the difficulty of forming a good low-impedance connection to the body with a reasonably sized low-cost electrode. Hence, the 60-Hz common-mode signal, which can be abstracted by a Thevenin equivalent signal $V_{60 \text{ Hz}}$ in series with the input impedance of the interferer Z_{intf} , still results in a relatively large common-mode signal of value $V_{\text{CM}}^{\text{body}} = V_{60 \text{ Hz}}(Z_{\text{gnd}}/(Z_{\text{intf}} + Z_{\text{gnd}}))$ on the body. The rejection of this large common-mode signal requires a differential amplifier with very good common-mode rejection to ensure that the tiny differential EKG signal is not drowned by the large common-mode signal. Passive grounding also requires an amplifier with a large input common-mode operating range to avoid saturation effects. Building an amplifier with a large common-mode input operating range is deleterious to low-power operation because it makes a large power-supply voltage necessary. Winter and Webster [12] showed that active grounding, wherein the third grounding electrode is actively driven to be at the common-mode value of the main differential-input electrodes, yielded reliably superior performance for measuring biopotential signals. This advantage arises because the common-mode signal is attenuated to a value

$$V_{\text{CM}}^{\text{body}} = V_{60 \text{ Hz}} \frac{\frac{Z_{\text{gnd}}}{1+A_{lp}}}{\frac{Z_{\text{gnd}}}{1+A_{lp}} + Z_{\text{intf}}} \quad (1)$$

where A_{lp} is the feedback loop gain of the common-mode feedback loop. If A_{lp} is sufficiently large at 60 Hz, the common-mode rejection and power-supply voltage requirements on the main differential amplifier are relaxed because the common-mode signal is considerably attenuated. Active grounding with common-mode feedback (CMFB) in the context of an EKG is described in [11] but without attention to low-power operation. Due to its advantages for common-mode noise rejection and low-power operation, we chose to build our low-power EKG amplifier with common-mode feedback or active grounding as well.

Our low-power performance is not achieved due to a single technique. Rather, it is due to multiple design choices that allocate power and area resources amongst various stages of the amplifier in a fashion that efficaciously combats thermal noise, common-mode 60-Hz noise, $1/f$ noise and device mismatch such that power consumption is optimally low without sacrificing performance. This paper is organized as follows: In Section II, we describe the design of the amplifier. In Section III, we present a feedback block diagram representation of our amplifier. In Section IV, we analyze the common-mode rejection of the amplifier. In Section V, we analyze its noise and noise-power tradeoffs. In Section VI, we present experimental measurements including the recording of an electrocardiogram trace. In Section VII, we conclude by summarizing our contributions.

II. AMPLIFIER DESIGN

The amplifier, designed in a 0.5- μm AMI process provided by MOSIS, makes use of subthreshold complementary metal-oxide semiconductor (CMOS) circuits in order to maximize transconductance for a given power level. To robustly bias all of the devices, we make use of the current reference

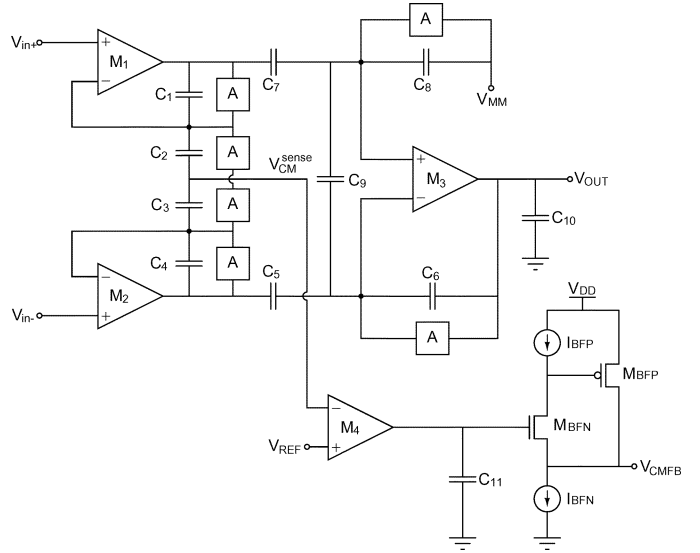


Fig. 2. Electrocardiogram amplifier schematic.

described in [13]. Additionally, we work with a center-tapped voltage supply with rails at 3 V and 1.5 V. While the half-rail supply saves power when extra headroom is unnecessary, the 3-V supply increases dynamic range at the output and helps accommodate the input common-mode operating range. Since RF-powered tags usually incorporate a few stages of charge pumping to achieve an output voltage [3], intermediate output stages of the charge pump may be used to generate a 1.5-V supply while the final output stage of the charge pump may be used to generate the 3-V supply if our amplifier is used in radio-frequency identification (RFID) systems. In battery-powered systems, the center connection of two 1.5-V batteries in series can generate the 1.5-V supply while the series addition generates the 3-V supply.

A. Instrumentation–Amplifier Topology

The core of the AFE is a two-stage instrumentation amplifier (see Fig. 2). It may seem that a second stage adds power and noise. However, the following advantages and flexibility in the instrumentation topology more than compensate for these shortcomings.

- 1) Gain distribution. By spreading amplification between two stages, the gain requirement of each stage is reduced. The two-stage strategy removes the need to cascode for high gain and thereby allows the use of a half-rail supply.
- 2) Common-mode rejection. The extra stage in the instrumentation amplifier boosts CMRR [14].
- 3) Common-mode extraction. Common-mode feedback requires that the common-mode of the input signals be extracted. An instrumentation-amplifier topology provides this automatically as it is inherent to the topology: the voltage $V_{\text{CM}}^{\text{sense}}$ in Fig. 2 provides common-mode information.
- 4) Multiple degrees of freedom. An instrumentation-amplifier provides us with more flexibility for power minimization than a single-stage amplifier because it has more degrees of freedom that can be exploited for optimization.

B. OTA Design

The basic building blocks of the instrumentation amplifier are the three operational transconductance amplifiers (OTAs), which we implement as long-tailed pairs with current mirror loads (Fig. 4). Although the topology is simple, several important optimizations can improve performance as follows.

- 1) PMOS devices. Flicker noise is one to two orders of magnitude smaller for PMOS devices than NMOS devices [15]. We therefore use PMOS input devices for all amplifiers.
- 2) Input transistor sizing. By increasing W/L , the input transistors in the first-stage are driven deep into subthreshold, where transconductance is maximized. They are also made large so as to reduce flicker noise.
- 3) Load transistor sizing. Load devices in the first-stage amplifiers are driven above threshold by decreasing W/L . This reduces their drain current noise considerably.
- 4) Device matching. The second-stage amplifier is not as important for noise performance. Therefore, the input and load devices are sized to assist common-centroid layout and matching.

These different sizing strategies would have not been possible in a single-stage amplifier.

C. Capacitor-Based Amplification

The standard instrumentation amplifier uses ratios of feedback resistors to precisely set gain values. Resistors have relatively poor matching properties, introduce noise, and usually require many microamps of current to drive, unless they are quite large, which is costly in terms of area. Therefore, we use capacitors to set gains in the instrumentation amplifier. Even moderate-sized poly-poly capacitors in our process can be matched to within 1% with a careful unit-cell-based layout [16]. Capacitors also do not add noise.

Capacitors cannot provide a pathway for dc current to flow. To establish a dc operating point, we use “adaptive elements,” first described in [17] and later applied to neural amplifiers [18] and ultra-low-power neural amplifiers [19]. Such adaptive elements function as back-to-back diodes, shown as the “A” blocks in Fig. 2. They effectively implement resistances of a very large value and establish the dc operating point of the circuit but allow the capacitances in parallel with them to determine ac gain at all but extremely low ac frequencies [17].

D. Common-Mode Feedback

Passive grounding connects a ground electrode on the body, typically on the leg, via a skin electrode or “dermatrode” whose impedance has a magnitude of approximately 50 k Ω . Active grounding via CMFB circuitry attenuates the impedance of this grounding connection by a factor that is approximately the reciprocal of the common-mode feedback loop gain. An extremely high loop gain is deleterious for stability and power consumption, however, and, therefore, needs to be chosen with these concerns in mind as well. Noise from the common-mode amplifier is well rejected by the topology due to its inherently high CMRR and presents less of a concern.

Since the CMFB amplifier must drive a relatively small impedance, a voltage buffer is required between the CMFB

OTA output and the grounding leg electrode. This buffer has two main requirements.

- 1) Any current sourced to the body to negate common-mode interfering current via feedback has limits that are determined by the buffer’s bias current. The buffer therefore requires a certain minimum amount of bias current.
- 2) The buffer’s output impedance Z_{out} is in series with that of the electrode. The effect of common-mode feedback is then to replace the electrode impedance Z_e with $(Z_e + Z_{out})/(A + 1)$, where A is the loop gain of the common-mode feedback loop. The buffer’s output impedance should therefore be made small relative to the electrode impedance. Any further reductions significantly below this value compromise power without improving performance.

There is no way to avoid the first of these requirements. Our experiments revealed that a 0.5 μ A–0.6 μ A bias current in the buffer was sufficient to negate even large interfering common-mode signals and meet the first requirement: A 60-Hz interference current of 0.3 μ A on a 200-pF body capacitance to earth yields a 5-V interference signal that can be measured on an oscilloscope. However, for a simple source-follower buffer biased at this level, the output impedance $Z_{out} = 1/g_m$ is comparable to the electrode impedance and the second requirement is not satisfied. We solved this issue by using a super source-follower (SSF) instead, as revealed by the transistor-and-current-source circuit of Fig. 2 and analyzed in detail in [20]. The SSF leverages one more transistor and negligible additional current to have the output conductance of the SSF in Fig. 2 approximately given by $g_m^{MBFP}(g_s^{MBFN}r_o^{MBFN} + 1)$, where g_s and r_o are small-signal source transconductance and small-signal drain-to-source resistance parameters of transistor M_{BFN} . With these circuits in place, the electrode impedance and loop stability become limiting factors in CMFB efficiency. Our experimental results, which are described in detail in Section VI, showed that the common-mode feedback attenuated our common-mode signal by 33 dB, compared with a simple feedforward amplification strategy that has no common-mode feedback.

Standard diode-resistor circuits can limit the current output by the common-mode feedback circuit on the body [12] and our low-power design with microamps of current consumption is inherently safe and unperturbed by the inclusion of such circuits.

E. Power Distribution

The AFE consists of four power-consuming modules: the first amplifier stage, the second amplifier stage, the CMFB amplifier, and the CMFB buffer. We examine the power requirements of each in turn.

- 1) The bias current in the first-stage amplifiers M_1 and M_2 defines the noise of the system. It is therefore optimal to allocate much of the AFE power here.
- 2) The second-stage amplifier M_3 can be relatively noisy, since it has two orders of magnitude less impact on input-referred noise than M_1 or M_2 . Very little power may therefore be allocated to this stage.

TABLE I
 VOLTAGE AND CURRENT ALLOCATIONS

First stage	1.5V	0.6 μ A
Second stage	3V	0.1 μ A
CMFB amplifier	3V	0.1 μ A
CMFB buffer	1.5V	0.6 μ A

- 3) The CMFB amplifier can also be relatively noisy and, therefore, low power, since common-mode noise is inherently well rejected in the overall circuit topology.
- 4) The CMFB buffer requires a bias current in excess of 0.5 μ A. Without this current, it will be unable to quench the common-mode interfering currents that are typically under 0.1 μ A but could potentially be larger.

Power is also influenced by the choice of supply voltages. The first-stage amplifier and the CMFB buffer do not require 3 V of headroom. We can therefore cut their power consumption in half by using a 1.5-V supply. Fortunately, they are also the most power-hungry modules. Voltage and current allocations for our design are summarized in Table I. Immunity to RF interference requires filters on the power supply as described in [21] but were not implemented in this version.

III. BLOCK DIAGRAM

Fig. 3 shows a feedback block diagram that represents all sources of signal and noise in the EKG amplifier of Fig. 2. The block diagram is useful for analyzing the noise and CMRR of the amplifier, which are described in more detail in Sections IV and V. Here, we shall focus on describing how Fig. 2 maps to Fig. 3.

The input signal to the amplifier may be described as a common-mode signal V_{CM}^{body} that is added to $v_{EKG}/2$ to generate V_{in+} and to $-v_{EKG}/2$ to generate V_{in-} in Figs. 2 and 3. The differential signal $v_{EKG} = v_{EKG}/2 - (-v_{EKG}/2)$ is what we would like to amplify and the common-mode signal V_{CM}^{body} is what we would like to reject. The noise sources v_n^{M1} and v_n^{M2} are the net input-referred voltage noise per unit bandwidth of the M_1 and M_2 amplifiers, respectively, and are represented by “crooked-line” noisy inputs to adder blocks in Fig. 3. We shall use the convention of representing all noise sources in Fig. 3 by similar crooked-line inputs to remind us of the noisy nature of these inputs. As the positive input and the negative input of the M_1 amplifier are nearly equal to each other because of negative feedback, and similarly, the positive and negative input of the M_2 amplifier are nearly equal to each other, the sensed common-mode voltage V_{CM}^{sense} in Fig. 3 is given by a simple capacitive-divider relation with C_2 and C_3 forming the capacitive divider and V_{in+} and V_{in-} forming the inputs to the divider. The value of V_{CM}^{sense} in Fig. 3 represents this capacitive-divider relation. Note that if the capacitors C_2 and C_3 are not perfectly matched, there is a slight gain error in the determination of the common-mode voltage such that $V_{CM}^{sense} \neq V_{CM}^{body}$. The value of V_{CM}^{sense} is compared with V_{REF} in the amplifier M_4 to create an error signal, which causes the CMFB amplifier M_4 to output an integrator error-correction output onto the capacitance C_{11} in Fig. 2, which is represented by the (G_M^{M4}/sC_{11}) block in Fig. 3. The input-referred noise per unit bandwidth of the common-mode amplifier M_4 is

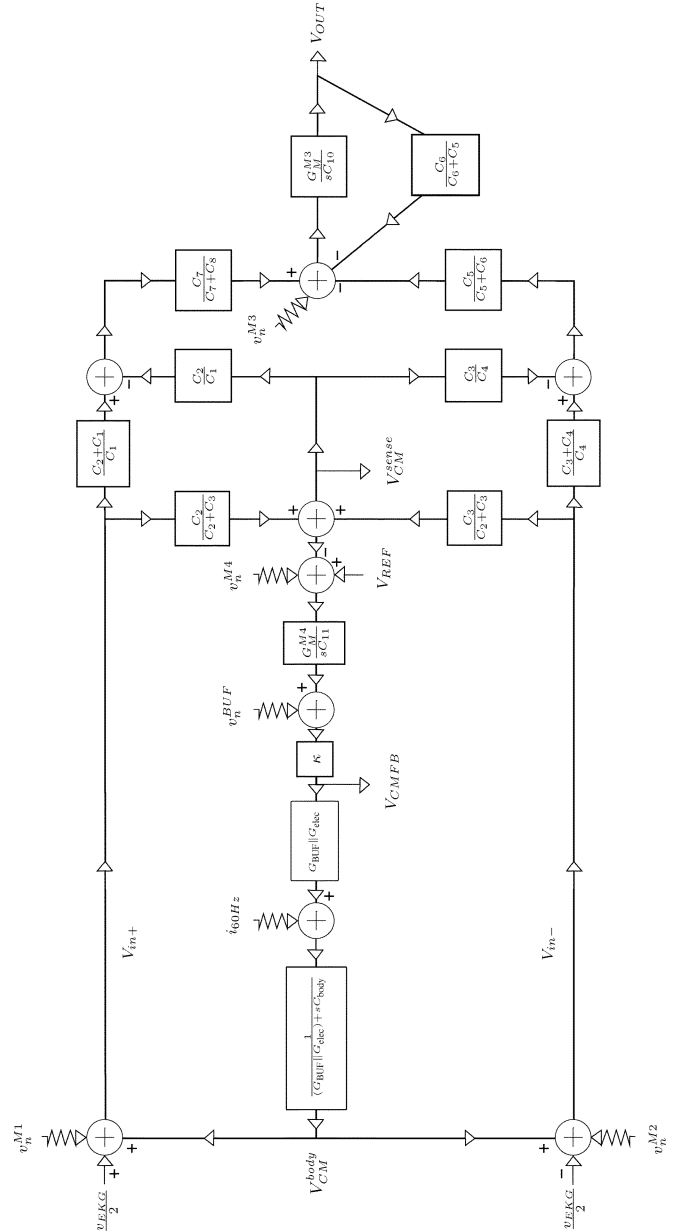


Fig. 3. Block diagram. Jagged arrows denote noise sources.

represented by the v_n^{M4} input in Fig. 3. The output of the CMFB amplifier is fed to the SSF circuit in Fig. 2, which has a gain of slightly less than 1.0 due to the body effect of M_{BUF} . The SSF’s output resistance R_{BUF} adds in series with the grounding leg-electrode impedance R_{elec} to contact the body, which is empirically well approximated by a Norton equivalent comprised of $i_{60\text{ Hz}}$ in parallel with a capacitive impedance of approximately $C_{body} = 200$ pF to ground. With a little bit of algebra, the SSF circuit, including the input-referred voltage noise per unit bandwidth of the SSF v_n^{BUF} and the electrode connections to the body can therefore be represented by the blocks between the (G_M^{M4}/sC_{11}) integrator and V_{CM}^{body} in Fig. 3. The common-mode feedback loop from V_{CM}^{body} to V_{CM}^{body} is now completely represented. Note that we have used a conductance representation in Fig. 3 with $G_{BUF} = 1/R_{BUF}$ and $G_{elec} = 1/R_{elec}$. For simplicity, we have approximated the

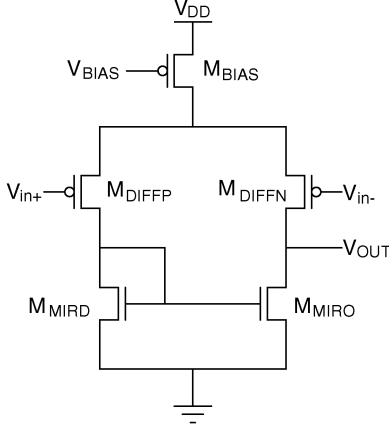


Fig. 4. Schematic of the operational transconductance amplifier (OTA) used four times in the EKG amplifier.

electrode impedance as being merely resistive, although it has reactive components as well.

The M_1 and M_2 amplifiers in Fig. 2 amplify the V_{in+} and V_{in-} inputs in Fig. 2 by $(C_2 + C_1)/C_1$ and $(C_3 + C_4)/C_4$, respectively, due to the noninverting configuration of these inputs. The V_{CM}^{sense} input at the middle of C_2 and C_3 is amplified by the M_1 and M_2 amplifiers by $-C_2/C_1$ and $-C_3/C_4$, respectively, due to the inverting configuration of this input. Thus, Fig. 3 represents the first stage of differential amplification by M_1 and M_2 by corresponding adder and gain blocks in Fig. 3. Note that since V_{CM}^{sense} is very nearly V_{CM}^{body} , the gain of M_1 to V_{CM}^{body} is very nearly $(C_2 + C_1)/C_1 - (C_2/C_1) = 1$ if we sum contributions from noninverting and inverting paths. Similarly, the gain of M_2 to V_{CM}^{body} is very nearly $(C_3 + C_4)/C_4 - (C_3/C_4) = 1$. Since amplifier M_3 and the capacitors associated with it take the amplified difference of the outputs of M_1 and M_2 with gain A_{2ndstg} , V_{CM}^{body} has a gain of nearly $A_{2ndstg} \cdot (1 - 1) \approx 0$ to the final output of M_3 such that the common-mode gain of the topology is nearly zero. In practice, capacitance mismatches in the second-amplification stage, and to a lesser extent, in the first-amplification stage, limit the common-mode gain to a nonzero value.

The differential amplifier formed by M_3 and associated capacitances that create the second stage of amplification in Fig. 2 are represented by the rightmost gain and adder blocks of Fig. 3. The input-referred voltage noise per unit bandwidth of M_3 is conveniently represented by an adder input. Fig. 3 shows if $C_7/(C_7 + C_8) = C_5/(C_5 + C_6)$, then the second gain stage provides differential amplification that can be derived by Black's feedback formula to be

$$A_{2ndstg} = \frac{C_5}{C_6}. \quad (2)$$

Thus, the overall differential gain of the amplifier is given by

$$\begin{aligned} A_{diff} &= A_{1ststg} \cdot A_{2ndstg} \\ &= \left(\frac{C_2 + C_1}{C_1} \right) \left(\frac{C_5}{C_6} \right) \\ &= \left(\frac{C_3 + C_4}{C_4} \right) \left(\frac{C_7}{C_6} \right) \end{aligned} \quad (3)$$

if there is perfect capacitor matching between the two differential halves of the signal processing in both stages of amplification.

IV. CMRR ANALYSIS

Due to the large amount of 60-Hz hum in biopotential measurements, common-mode rejection is as important as low-noise operation. Ideally speaking, the differential form of the instrumentation amplifier should prevent any and all common-mode signals from bleeding into the output. However, transistors are never perfectly matched, mirrored current sources have finite output impedance, and capacitors have nonzero tolerances. All of these effects contribute to a finite CMRR.

Assuming that the feedback-amplifier loops involving M_1 , M_2 , and M_3 in Fig. 2 operate with sufficient loop gain so that closed-loop gains are determined only by capacitances, and that C_2 and C_3 are not perfectly matched, i.e.,

$$\alpha = \frac{C_2}{C_2 + C_3} \neq \frac{1}{2} \quad (4)$$

then

$$\begin{aligned} V_{CM}^{sense} &= \alpha \left(V_{CM}^{body} + \frac{v_{EKG}}{2} \right) + (1 - \alpha) \left(V_{CM}^{body} - \frac{v_{EKG}}{2} \right) \\ &= V_{CM}^{body} + \left(\alpha - \frac{1}{2} \right) v_{EKG}. \end{aligned} \quad (5)$$

From Fig. 3 and (5), we then find that

$$\begin{aligned} V_{OUT} &= \frac{C_7}{C_7 + C_8} \frac{C_6 + C_5}{C_6} \left(V_{CM}^{body} - \frac{C_2}{C_1} \left(\alpha - \frac{1}{2} \right) v_{EKG} \right. \\ &\quad \left. + \frac{v_{EKG}}{2} \frac{C_1 + C_2}{C_1} \right) \\ &\quad - \frac{C_5}{C_5 + C_6} \frac{C_6 + C_5}{C_6} \left(V_{CM}^{body} - \frac{C_3}{C_4} \left(\alpha - \frac{1}{2} \right) v_{EKG} \right. \\ &\quad \left. + \frac{v_{EKG}}{2} \frac{C_3 + C_4}{C_4} \right). \end{aligned} \quad (6)$$

Some algebraic simplification of (6) and substitution of the value of α from (4) then yields

$$\begin{aligned} V_{out} &= \frac{C_6 + C_5}{C_6} \left(\frac{C_7}{C_7 + C_8} - \frac{C_5}{C_5 + C_6} \right) V_{CM}^{body} \\ &\quad + \frac{1}{2} \frac{C_6 + C_5}{C_6} \left(\frac{C_7}{C_7 + C_8} \frac{C_1 + C_2}{C_2} \right. \\ &\quad \left. + \frac{C_5}{C_5 + C_6} \frac{C_3 + C_4}{C_3} \right) v_{EKG} \\ &\quad - \frac{1}{2} \frac{C_6 + C_5}{C_6} \frac{C_2 - C_3}{C_2 + C_3} \\ &\quad \times \left(\frac{C_2}{C_1} \frac{C_7}{C_7 + C_8} - \frac{C_3}{C_4} \frac{C_5}{C_5 + C_6} \right) v_{EKG}. \end{aligned} \quad (7)$$

The coefficient of v_{EKG} in the third row of (7) is very small when compared with the coefficient of v_{EKG} in the second row of (7): the third-row coefficient is determined by product terms that are composed of capacitor-gain differences that nearly cancel while the second-row coefficient is determined by product terms that are composed of capacitor-gain sums that

add. Thus, if we neglect the third-row term, we find that the CMRR, the ratio of the coefficients of the v_{EKG} , and V_{CM}^{body} terms in (7) are given by

$$\text{CMRR} = \frac{\frac{C_7}{C_7+C_8} \frac{C_1+C_2}{C_2} + \frac{C_5}{C_5+C_6} \frac{C_3+C_4}{C_3}}{2 \left(\frac{C_7}{C_7+C_8} - \frac{C_5}{C_5+C_6} \right)}. \quad (8)$$

We observe from the denominator of (8) that it is the matching between capacitances in the second stage of the instrumentation amplifier that is the key determining factor in the CMRR of the overall topology. The first-stage common-mode gain is always 1 in each differential half independent of capacitance since both M_1 and M_2 attempt to drive their negative inputs to the common-mode input voltage in Fig. 2. Thus, common-mode signals from the first stage should be perfectly cancelled out by the differential second stage if second-stage matching is perfect [14]. However, this is clearly not the case. Even with ideal capacitor matching in the second stage, due to finite loop-gain effects in the M_1 and M_2 amplifiers, which can be mismatched between M_1 and M_2 , and finite common-mode effects within each of M_1 and M_2 , which also can be mismatched, the common-mode response will always slightly differ between the output of M_1 and M_2 . This difference will then be amplified by the second stage. Similarly, if M_3 has finite CMRR, even with perfect matching in all other parameters of the topology, the CMRR of the topology will then be equal to the CMRR of M_3 . Thus, (8) only represents an upper bound on the CMRR that is due to capacitor matching in the second stage, likely the most important determinant of the CMRR of our topology.

If common-mode feedback is present, the common-mode feedback loop shown in Fig. 3 attempts to maintain V_{CM}^{body} at V_{REF} . The loop transmission $L_{\text{CMFB}}(s)$ of this feedback loop is given by

$$L_{\text{CMFB}}(s) = \kappa \left(\frac{G_M^{M4}}{sC_{11}} \right) \frac{G_{\text{BUF}} \| G_{\text{elec}}}{G_{\text{BUF}} \| G_{\text{elec}} + sC_{\text{body}}}. \quad (9)$$

At frequencies $s = j\omega$ including 60 Hz, where the loop gain is sufficiently high, the transfer function from $i_{60 \text{ Hz}}$ to V_{CM}^{body} in Fig. 3 is well approximated by the reciprocal of the feedback path transmission so that

$$\begin{aligned} V_{CM}^{\text{body}} &= \frac{i_{60 \text{ Hz}}}{G_{\text{BUF}} \| G_{\text{elec}} (2\pi j \cdot 60)} \frac{C_{11} \cdot 2\pi 60}{\kappa G_M^{M4}} \\ &\approx \frac{i_{60 \text{ Hz}}}{G_{\text{elec}} (2\pi j \cdot 60)} \frac{2\pi 60}{\kappa \omega_{\text{CMFB}}}. \end{aligned} \quad (10)$$

Thus, it is advantageous to have a large loop crossover frequency ω_{CMFB} in the common-mode feedback loop to attenuate the value of V_{CM}^{body} . However, ω_{CMFB} must be at least a factor of 4 less than $(G_{\text{BUF}} \| G_{\text{elec}}) / C_{\text{body}}$ for the CMFB loop to be overdamped and exhibit no ringing in its step response. A large value of G_M^{M4} , which can achieve a high ω_{CMFB} is also deleterious for power consumption. Our design choices for biasing M_4 were informed by these considerations. The capacitance C_{11} can be fairly small because common-mode noise is inherently attenuated by the instrumentation-amplifier topology.

It is interesting to note that Fig. 3 yields noise transfer functions via Black's formula for all noise sources (e.g., it allows us

to note that the noise power spectrum of v_n^{BUF} is highpass filtered until the crossover frequency while that of v_n^{M4} is not) so that the v_n^{M1} and v_n^{M2} sources directly affect the minimum detectable signal and that the noise source at v_n^{M3} is reflected back to the input with a gain of $((C_8 + C_7) / C_7) (C_1 / (C_1 + C_2))$, etc. It also allows us to see that all common-mode noise sources, such as v_n^{BUF} , v_n^{M4} , or $i_{60 \text{ Hz}}$ have inherently low transfer functions to the output due to their attenuation in the common-mode feedback loop and because of symmetric cancellation between the two differential halves.

V. NOISE ANALYSIS

The total thermal current noise power at the output of an OTA can be calculated by adding the noise current powers from each transistor. The bias-current transistor does not contribute to this sum. The input stage devices, which operate in the subthreshold regime with bias current I_b , produce current noise power given by [22]

$$\overline{|i_n|^2} = 2qI_b \Delta f. \quad (11)$$

The load transistors, which are sized to operate above threshold, produce current noise power given by [23]

$$\overline{|i_n|^2} = \frac{8}{3} kT g_m \Delta f. \quad (12)$$

Adding the contributions from each transistor yields the output current noise i_n^{Mj} for OTA M_j

$$\overline{|i_n^{Mj}|^2} = \left(4qI_b + \frac{16}{3} kT g_m^{Mj} \right) \Delta f. \quad (13)$$

Combining the contributions from each OTA can then produce the input-referred thermal noise voltage for the overall amplifier

$$\begin{aligned} \overline{|v_{ni}|^2} &= \frac{\overline{|i_n^{M1}|^2}}{(G_m^{M1})^2} + \frac{\overline{|i_n^{M2}|^2}}{(G_m^{M2})^2} + \frac{\overline{|i_n^{M3}|^2}}{(G_m^{M3})^2} \\ &\quad \times \frac{1}{(A_{1\text{ststg}}(1 + 1/A_{2\text{ndstg}}))^2} \end{aligned} \quad (14)$$

where we make use of the following definitions.

- 1) i_n^{Mj} is the output current noise from OTA M_j ;
- 2) G_m^{Mj} is the transconductance of OTA M_j ;
- 3) $A_{1\text{ststg}}$ and $A_{2\text{ndstg}}$ are the gains of the first and second stages, respectively.

Each of the first-stage OTAs M_1 and M_2 is predicted to contribute $115 \text{ nV}/\sqrt{\text{Hz}}$ to input-referred noise. Since $A_{1\text{ststg}}$ is on the order of 20, second-stage noise power is divided by a factor of 400 and the third term may be ignored—even though M_3 may be significantly noisier than M_1 or M_2 .

From the block diagram of Fig. 3, we notice that common-mode noise sources, such as v_n^{M4} and v_n^{BUF} couple almost symmetrically to the two differential halves, and get subtracted at the final output to generate a residue limited only by the matching of the two differential halves. Therefore, they contribute negligibly to the input-referred differential noise of the amplifier to first order. In addition, the common-mode feedback loop attenuates such noise sources even further. Thus, to first order, we can

TABLE II
EKG PERFORMANCE

Power	2.76 μ W
Gain	45.3 dB
Bandwidth	290 Hz
Dynamic Range	41.8 dB
Noise	8.1 μ V _{rms}
CMRR at 60 Hz	90 dB

assume that the contribution of all common-mode noise sources is negligible in determining the input differential minimum-detectable signal of the amplifier.

The total input referred thermal noise is then computed to be 162 nV/ $\sqrt{\text{Hz}}$ or 3.24 μ V_{rms} over the expected amplifier signal bandwidth of 300 Hz. The remainder is due to flicker ($1/f$) noise. Because of its dependency on process, the contribution of $1/f$ is difficult to predict, but its analytical effect can be calculated [24]. The magnitude of $1/f$ noise is reduced as far as possible by using large PMOS input devices [24]. One might reduce its contribution even further by means of chopper-stabilization, as in [6].

VI. MEASURED PERFORMANCE

The AFE was fabricated in an AMI 0.50- μ m C5 process through the MOSIS prototyping service (see Fig. 10 for a photograph). To increase experimental flexibility, bias currents for M_1, M_2, M_3, M_4 , and the super-source-follower were controlled by digitally selected binary weighted current sources. Half- and full-rail power was supplied by independent voltage sources (in practice, this power may be obtained by the intermediate and final stages of a charge pump, or by the center and end connections of two 1.5-V batteries). The center tap for the voltage source slightly increased from 1.5 V to 1.8 V to accommodate a larger than expected common-mode range. The additional headroom prevents the super buffer from saturating and producing a nonlinear output. Following the increase, the AFE was found to consume 2.76 μ W of power. Table II summarizes the overall experimental performance of our amplifier.

In addition to isolated testing of the AFE, EKG measurements were obtained from a subject. FS-TB1 hydrogel electrodes from Skintact, attached to a leg and both arms, were connected to the corresponding terminals of the AFE. The connecting wires were twisted together as much as possible to reduce interference from 60-Hz hum. Several periods of a captured EKG waveform are shown in Fig. 5. The amplifier's relatively low-noise levels and use of common-mode feedback allow all of the important features of the EKG—the P, Q, R, S, and T waves—to be observed.

To measure gain and bandwidth of the amplifier, one input was connected to V_{REF} , the other to V_{REF} plus a small ac signal v_{EKG} , and the common-mode feedback output was left unconnected. The measured gain and bandwidth, at 45.3 dB and 290 Hz, were in line with simulation. See Fig. 6 for the frequency response.

To measure CMRR, the inputs were first connected together into a single input node. A small ac common-mode signal and the CMFB output of the AFE were connected to this node by resistors R_{CM} and R_{CMFB} , respectively. The relative

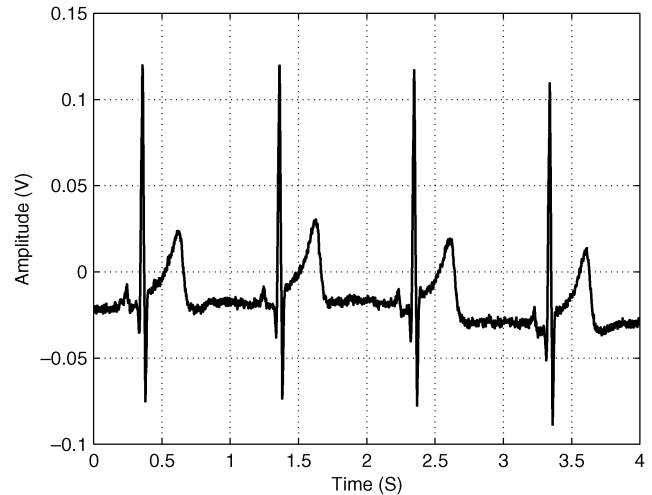


Fig. 5. Sample EKG signal captured with the amplifier from a subject with a healthy heart.

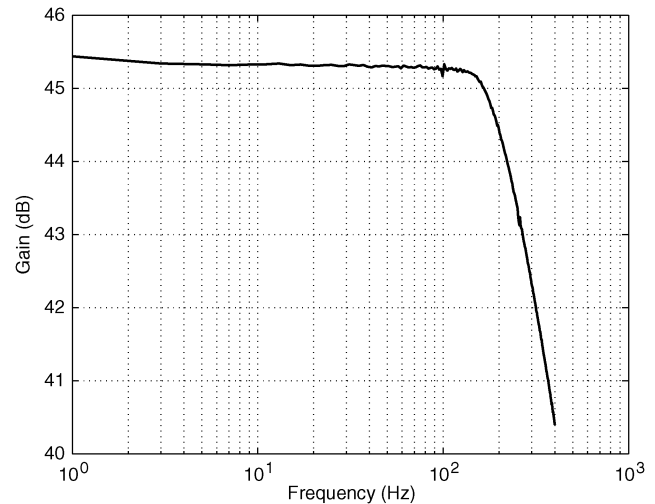


Fig. 6. Measured frequency response of the amplifier.

sizes of R_{CM} and R_{CMFB} determine the effectiveness of common-mode feedback. For instance, if R_{CM} were zero, then common-mode feedback would be unable to attenuate the input common-mode signal. Although in reality, the impedance to the interference source, represented by R_{CM} , is likely to be more than the impedance of the leg electrode, represented by R_{CMFB} , we conservatively set $R_{\text{CM}} = R_{\text{CMFB}} = 100 \text{ k}\Omega$ for common-mode measurements.

At 90 dB at 60 Hz, the CMRR is slightly higher than previously reported values [11], [25]. Nonetheless, this number falls short of the 114 dB expected from design and simulation. The 114 dB of simulated CMRR consists of roughly 34 dB from CMFB, 40 dB from gain in the amplifier, and 40 dB from common-mode rejection in the second-stage amplifier, under randomly selected 1% mismatch in capacitors. The source of the problem is not the common-mode feedback circuitry, which works entirely as expected (see Fig. 9). The actual bottleneck is likely capacitor mismatch in the second stage of the instrumentation amplifier as predicted by (8) in Section IV. The gap may

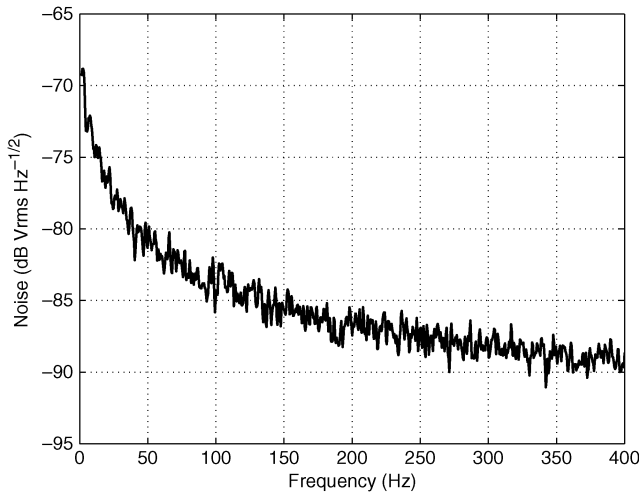


Fig. 7. Noise power spectral density of the amplifier.

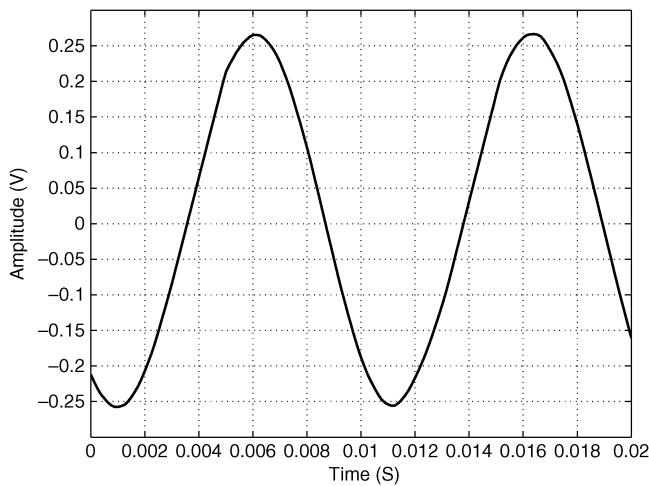


Fig. 8. The 100-Hz sine wave at the amplifier output. The measured THD is 4.4%.

be erased by more stringent layout and matching techniques targeting capacitors $C_5 - C_8$.

To measure noise, the inputs were first connected to one another as in the CMRR measurement to zero out the differential v_{EKG} inputs to the amplifier in Fig. 3. The resulting common input node was connected directly to a reference voltage V_{REF} , and the common-mode feedback loop was disconnected because common-mode noise makes a negligible contribution to the AFE's output. The output-power spectrum under these conditions divided by the differential gain of the amplifier yielded the input-referred noise spectrum (Fig. 7) and a total input-referred noise power of $8.1 \mu\text{V}_{\text{RMS}}$. Flicker noise is responsible for more than half this number; in future work, techniques, such as chopping and correlated double sampling, may be able to reduce this contribution. Since the largest undistorted (total harmonic distortion (THD) of less than 5%) sine wave at the amplifier's output had an amplitude of 0.5 V (Fig. 8), the dynamic range of the amplifier is 41.8 dB.

Input referring both this dynamic range and the noise floor, the amplifier can handle inputs of amplitude up to 4.1 mV with a resolution limited by $8.1 \mu\text{V}_{\text{RMS}}$ of noise. Since typical EKG

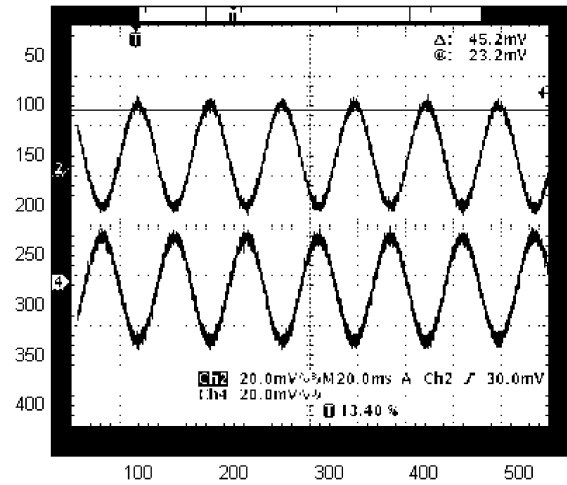


Fig. 9. Large common-mode signal is fed to the input of the amplifier (top). The CMFB amplifier drives the leg electrode in opposition in order to cancel this disturbance (bottom).

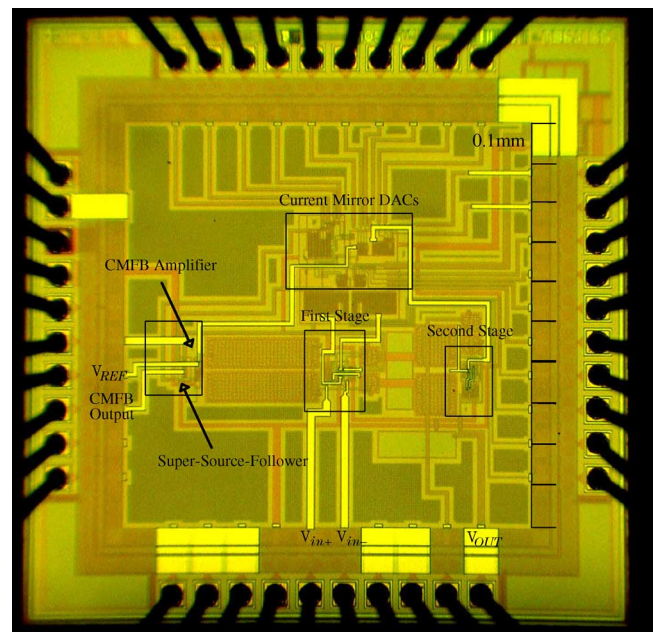


Fig. 10. Die photo of the fabricated AFE.

signals can range in amplitude from a few microvolts at their smallest features to a few millivolts during the QRS complex, our input dynamic range can handle almost all practical EKG signals of interest. As demonstrated in Fig. 5, our experimental measurements are sufficient to resolve the P wave.

VII. CONCLUSION

We have described an EKG amplifier with $8 \mu\text{V}$ of input-referred noise, 90-dB CMRR, less than $3 \mu\text{W}$ of power consumption, and good cardiac signal fidelity. These specifications are the cumulative effect of several subthreshold low-noise and low-power optimizations of a classic instrumentation-amplifier topology with added common-mode feedback. When paired with an efficient low-resolution/speed ADC and RF power link, this amplifier could enable wireless, battery-free EKG measurements powered by energy harvesting.

ACKNOWLEDGMENT

The authors would like to thank M. Baker for helpful suggestions and assorted advice, and the MOSIS Educational Program (MEP) for generously providing chip-fabrication resources.

REFERENCES

- [1] C. Park and P. H. Chou, "An ultra-wearable, wireless, low power ECG monitoring system," in *Proc. IEEE BioCAS, The British Library*, Nov. 29–Dec. 1, 2006, pp. 241–244.
- [2] T. R. F. Fulford-Jones, G.-Y. Wei, and M. Welsh, "A portable, low-power, wireless two-lead EKG system," in *Proc. IEEE 26th Annu. Int. Conf. Engineering in Medicine and Biology Soc.*, Sep. 2004, vol. 1, pp. 2141–2144.
- [3] S. Mandal and R. Sarpeshkar, "Low-power CMOS rectifier design for RFID applications," *IEEE Trans. Circuits Syst. I, Reg. Papers*, vol. 54, no. 6, pp. 1177–1188, Jun. 2007.
- [4] H. Y. Yang and R. Sarpeshkar, "A bio-inspired ultra-energy-efficient analog-to-digital converter for biomedical applications," *IEEE Trans. Circuits Syst. I, Reg. Papers*, vol. 53, no. 11, pp. 2349–2356, Nov. 2006.
- [5] M. D. Scott, B. E. Boser, and K. S. J. Pister, "An ultra-low power ADC for distributed sensor networks," in *Proc. 28th Eur. Solid-State Circuits Conf.*, Sep. 2002, pp. 255–258.
- [6] T. Denison, K. Consoer, W. Santa, A.-T. Avestruz, J. Cooley, and A. Kelly, "A $2 \mu\text{W}$ 100 nV/rHz chopper-stabilized instrumentation amplifier for chronic measurement of neural field potentials," *IEEE J. Solid-State Circuits*, vol. 42, no. 12, pp. 2934–2945, Dec. 2007.
- [7] R. Martins, S. Selberherr, and F. Vaz, "A CMOS IC for portable EEG acquisition systems," in *Proc. IEEE Instrumentation and Measurement Technology Conf.*, May 1998, vol. 2, pp. 1406–1410.
- [8] K. A. Ng and P. K. Chan, "A CMOS analog front-end IC for portable EEG/ECG monitoring applications," *IEEE Trans. Circuits Syst. I, Reg. Papers*, vol. 52, no. 11, pp. 2335–2347, Nov. 2005.
- [9] R. F. Yazicioglu, P. Merken, R. Puers, and C. Van Hoof, "A $60 \mu\text{W}$ 60 nV/Hz readout front-end for portable biopotential acquisition systems," in *Proc. IEEE Int. Solid-State Circuits Conf. Digest Tech. Papers*, Feb. 2006, pp. 109–118.
- [10] H. Wu and Y. P. Xu, "A 1 V $2.3 \mu\text{W}$ biomedical signal acquisition IC," in *Proc. IEEE Int. Solid-State Circuits Conf. Digest Tech. Papers*, Feb. 2006, pp. 119–128.
- [11] M. J. Burke and D. T. Gleeson, "A micropower dry-electrode ECG preamplifier," *IEEE Trans. Biomed. Eng.*, vol. 47, no. 2, pp. 155–162, Feb. 2000.
- [12] B. B. Winter and J. G. Webster, "Reduction of interference due to common mode voltage in biopotential amplifiers," *IEEE Trans. Biomed. Eng.*, vol. BME-30, no. 1, pp. 58–62, Jan. 1983.
- [13] S. Mandal, S. Arfin, and R. Sarpeshkar, "Fast startup CMOS current references," in *Proc. IEEE Int. Symp. Circuits Systems*, May 2006, p. 4.
- [14] M. A. Smither, D. R. Pugh, and L. M. Woolard, "CMRR analysis of the 3-op-amp instrumentation amplifier," *Electron. Lett.*, vol. 13, no. 20, p. 594, 1977, 29.
- [15] Y. Nemirovsky, I. Brouk, and C. G. Jakobson, "1/f noise in CMOS transistors for analog applications," *IEEE Trans. Electron Devices*, vol. 48, no. 5, pp. 921–927, May 2001.
- [16] A. Hastings, *The Art of Analog Layout*. Upper Saddle River, NJ: Prentice-Hall, 2001, pp. 254–306.
- [17] T. Delbruck and C. A. Mead, "Adaptive photoreceptor with wide dynamic range," in *Proc. IEEE Int. Symp. Circuits and Systems*, May–2 Jun. 1994, vol. 4, pp. 339–342.
- [18] R. R. Harrison and C. Charles, "A low-power low-noise CMOS amplifier for neural recording applications," *IEEE J. Solid-State Circuits*, vol. 38, no. 6, pp. 958–965, Jun. 2003.
- [19] W. Wattanapanitch, M. Fee, and R. Sarpeshkar, "An energy-efficient micropower neural recording amplifier," *IEEE Trans. Biomed. Circuits Syst.*, vol. 1, no. 2, pp. 136–147, Jun. 2007.
- [20] P. A. Gray, P. J. Hurst, S. H. Lewis, and R. G. Meyer, *Analysis and Design of Analog Integrated Circuits*. New York: Wiley, 2001.
- [21] R. Sarpeshkar, C. Salthouse, J.-J. Sit, M. W. Baker, S. M. Zhak, T. K.-T. Lu, L. Turicchia, and S. Balster, "An ultra-low-power programmable analog bionic ear processor," *IEEE Trans. Biomed. Eng.*, vol. 52, no. 4, pp. 711–727, Apr. 2005.
- [22] R. Sarpeshkar, T. Delbruck, and C. A. Mead, "White noise in MOS transistors and resistors," *IEEE Circuits Devices Mag.* [Online]. Available: <http://www.doi.org/10.1109/101.261888>
- [23] D. Johns and K. Martin, *Analog Integrated Circuit Design*. New York: Wiley, 1996.
- [24] R. Sarpeshkar, R. F. Lyon, and C. Mead, "A low-power wide-linear-range transconductance amplifier," *Analog Integr. Circuits Signal Process.*, vol. 13, no. 1–2, pp. 123–151, 1997.
- [25] M. J. Burke and C. Assambo, World Scientific Eng. Academy Soc.y (WSEAS), "An improved micro-power pre-amplifier for dry-electrode ECG recording," in *Proc. 11th WSEAS Int. Conf. Circuits*, Stevens Point, WI, 2007, pp. 234–239.



Leon Fay received the B.Sc. and M.Sc. degrees in electrical engineering from the Massachusetts Institute of Technology, Cambridge, in 2008.

Currently, he is a Research Engineer with SRI International, Menlo Park, CA, in the communications, radar, and sensors group. He is working on low-power wireless sensors for harsh environments, signal-processing techniques for radar image reconstruction, and algorithms for high-speed tracking with impulse radar.



Vinith Misra received the B.Sc. and M.Sc. degrees in electrical engineering from the Massachusetts Institute of Technology, Cambridge, in 2008, and is currently pursuing the Ph.D. degree in electrical engineering from Stanford University, Stanford, CA.

His research interests include signal processing, information theory, and mixed-signal circuits, with a focus on the intersection between theory and practice.



Rahul Sarpeshkar (SM'07) received the Bachelor's degrees in electrical engineering and physics from the Massachusetts Institute of Technology (MIT), Cambridge, and the Ph.D. degree from the California Institute of Technology (Caltech), Pasadena.

After completing the Ph.D. degree at Caltech, he joined Bell Labs as a member of the technical staff. Since 1999, he has been on the faculty of MIT's Electrical Engineering and Computer Science Department where he heads a research group on Analog VLSI and biological Systems, and is currently an

Associate Professor. His research interests include analog microelectronics, ultra-low power circuits and systems, biologically inspired circuits and systems, biomedical systems, feedback systems, neuroscience, and molecular biology.

Dr. Sarpeshkar has received several awards, including the Packard Fellow award given to outstanding faculty, the ONR Young Investigator Award, the National Science Foundation Career Award, the Indus Technovator Award, and the junior Bose award for excellence in teaching. He holds more than 25 patents and has authored many publications, including one that was featured on the cover of *Nature*.